Design of a Resonant Reactive Shielding Coil for Wireless Power Transfer System

Jingjing Sun
Min H. Kao EECS
The University of Tennessee
Knoxville, TN USA
jsun30@vols.utk.edu

Ruiyang Qin
Min H. Kao EECS
The University of Tennessee
Knoxville, TN USA
rqin1@vols.utk.edu

Jie Li
Min H. Kao EECS
The University of Tennessee
Knoxville, TN USA
jli94@vols.utk.edu

Daniel J. Costinett
Min H. Kao EECS
The University of Tennessee
Knoxville, TN USA
daniel.costinett@vols.utk.edu

Leon M. Tolbert
Min H. Kao EECS
The University of Tennessee
Knoxville, TN USA
tolbert@utk.edu

***Abstract*—An investigation of a resonant reactive shielding coil for wireless power transfer (WPT) systems is presented in this work. The shielding coil attenuates the magnetic field above and to the side of air-core WPT coils. A parameterized coil model is used to allow arbitrary circular winding geometry and current direction. Detailed modeling and mathematical calculations are provided, and an optimized design algorithm is proposed. The design method is validated using an experimental prototype shielding coil applied to a 3.03 MHz electric vehicle (EV) WPT system operating at 500 W output power. Experimental results show that the peak flux density on the top-center area of the coil is suppressed from 105 μT to 50 μT, and the magnetic field to the side of the vehicle is maintained well below the safety standard. In addition, effect of the shielding coil in WPT systems with metal and ferrite plates is investigated.**

***Index Terms*—WPT, resonant reactive shielding coil, EV**

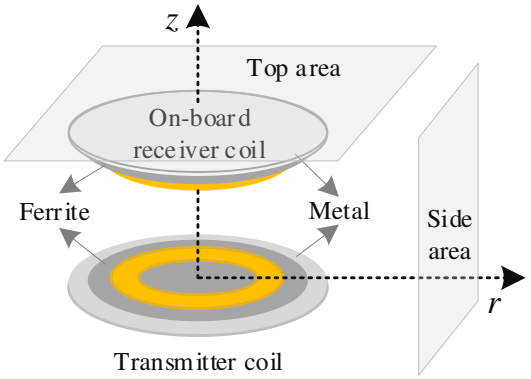

Fig. 1. Typical structure of the WPT system for EVs.

I. Introduction

Wireless power transfer (WPT) based on MHz magnetic resonant coupling has gained increasing attention in applications like consumer electronics and electric vehicles (EVs), due to the advantages of spatial freedom, long transfer distance, and high efficiency [1]–[3]. However, high-frequency ac current generates considerable stray magnetic field around the coils, especially in medium and high power EV applications with a large air gap between the transmitter coil (TX) and the receiver coil (RX) [4], [5]. This stray field generates core loss and eddy current loss in the surrounding ferrite and metal, and present human safety hazards outside the WPT coils. Health and safety standards for exposure to magnetic field are more stringent at high frequency range [6], [7].

As shown in Fig. 1, for a typical WPT system in EV applications, magnetic fields on both the side area and the top area should be maintained below safety limits for human exposure. Usually, metal and ferrite plates are implemented to help strengthen the coil coupling and shield the magnetic field. However, in the MHz magnetic resonant WPT system, conventional ferrite and metal based shielding degrades the system efficiency due to high core loss and eddy current loss. As an alternative, active shielding and passive shielding methods are studied [8]–[10]. Active shield with extra ac source provides good shielding performance, but consumes significant additional power and requires complex control or auxiliary circuitry [8], [9]. Compared with active shields, reactive shields with LC resonance can effectively reduce the magnetic field with simple implementation and low power loss [10].

Nevertheless, in EV applications, none of the alternative shielding methods can fully attenuate the stray magnetic field without ferrite/metal plates. To enhance the shielding effect and reduce the power loss, a hybrid shielding method with thin copper ring around the traditional Aluminum (Al) shield is proposed in [11]. However, only the field attenuation in the vehicle side area is considered, and the system efficiency improvement is limited. Therefore, more efficient shielding method is required, especially for medium and high power applications.

With the above considerations, this work investigates a design strategy of a resonant reactive shielding coil (SX) for an existing air-core WPT system to attenuate the magnetic field

above the coil and meet the safety standard on the side area. Also, shielding coil design in a 3 kW EV WPT system with Al and ferrite plates is investigated. The paper is organized as follows: Section II illustrates the proposed design strategy of the reactive shielding coil for an existing WPT system; Section III provides the experimental verification of the shielding coil; Section III shows the investigation and analysis of the shielding coil in WPT systems with ferrite/metal plates; Section V gives the conclusions.

II. Design Strategy of the Shielding Coil

A. Shielding Coil Model

The design procedure starts from defining the coil geometry, as presented in Fig. 2, where the shielding coil is represented by N loops with equal spacing above the receiver coil. In each loop, the number of winding turns can be zero or nonzero, and the winding direction can be clockwise or counterclockwise to stand for opposite current flow.

To adaptively represent the coil, a vector of current weighting factors for current magnitudes is defined as

$$\boldsymbol{T_{w,SX}} = [T_{w1}\ T_{w2}...T_{wn}...T_{wN}] \tag{1}$$

where $n = 1, 2, ...N$, T_{wn} represents the number of winding turns in Loop n, and $T_{wn} \in [-T_{w\_max}, T_{w\_max}]$, $T_{w\_max} \in \mathbb{Z}^+$. When $T_{wn} = 0$, there is no winding in Loop n; when $T_{wn} < 0$, there are $|T_{wn}|$ turns in Loop n each carrying current in a counterclockwise winding direction; when $T_{wn} > 0$, there are $|T_{wn}|$ turns in Loop n with clockwise winding direction. Equivalently, the shielding coil current is

$$\begin{aligned}\overrightarrow{\boldsymbol{i_{SX}}} &= [\overrightarrow{i_{SX1}}\ \overrightarrow{i_{SX2}}...\overrightarrow{i_{SXn}}..\overrightarrow{i_{SXN}}]_{1\times N} \\ &= \boldsymbol{T_{w,SX}}\overrightarrow{i_{m\_u}} \\ &= \boldsymbol{T_{w,SX}} I_{m\_u}\angle\phi_{SX}\end{aligned} \tag{2}$$

where $\overrightarrow{i_{m\_u}}$ is the designated base current at the terminals of the coil, and ϕ_{SX} is the current phase angle. In this way, design of the shielding coil structure and current is simplified to the sweep of the current vector and phase angle.

The physical position of the shielding coil is constrained by the inner radius r_{inner}, outer radius r_{outer}, and the air gap d_{SR} with the receiver coil. Since the shielding coil aims to attenuate the magnetic field on the top area and limit the flux density on the side area under the standard, a top boundary at $z = d_{z\_top}$ and a side boundary at $r = d_{r\_side}$ are defined, at which magnetic field will be checked to evaluate the shielding performance.

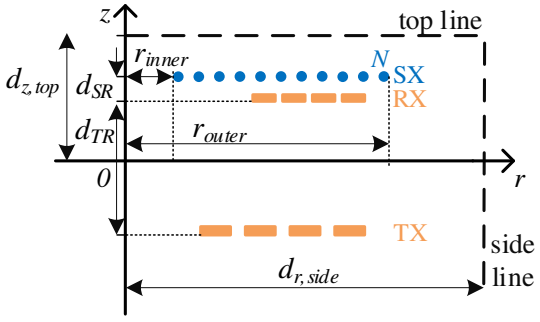

Fig. 2. The cylindrical view of the WPT coils.

B. Unit Permeance Matrices and Flux Density Matrices

For an existing WPT system, the transmitter coil self-inductance L_{TX}, the receiver coil self-inductance L_{RX}, and the mutual inductance between the transmitter coil and receiver coil M_{TR} are known. To calculate coil inductances and the magnetic field of the system with the shielding coil, unit permeance matrices between the shielding coil and the transmitter/receiver coils, and flux density matrices of the three coils are required.

In this model, the shielding coil self-inductance matrix is defined as

$$\boldsymbol{L_{SX\_u}} = \begin{bmatrix} L_{SX1} & M_{SX12} & .. & M_{SX1N} \\ M_{SX21} & L_{SX2} & .. & M_{SX2N} \\ : & : & : & : \\ M_{SXN1} & M_{SXN2} & .. & L_{SXN} \end{bmatrix}_{N\times N} \tag{3}$$

where L_{SXn} is the self-inductance of one winding turn in the shielding coil Loop n, M_{SXnm} is the mutual inductance between winding turns in Loop n and Loop m. Accordingly, the equivalent series resistance (ESR) matrix of the shielding coil is $\boldsymbol{R_{SX\_u}} = [R_{SX1}\ R_{SX2}...R_{SXn}...R_{SXN}]_{1\times N}$, where R_{SXn} is the resistance of one winding turn in Loop n of the shielding coil. The unit mutual inductance matrices between the shielding coil and the transmitter/receiver coils are defined as

$$\boldsymbol{M_{TS\_u}} = [M_{TS1}...M_{TSn}...M_{TSN}]_{1\times N} \tag{4}$$

$$\boldsymbol{M_{RS\_u}} = [M_{RS1}...M_{RSn}...M_{RSN}]_{1\times N} \tag{5}$$

where M_{TSn} represents the mutual inductance between the transmitter coil and one winding turn in Loop n of the shielding coil, M_{RSn} represents the mutual inductance between the receiver coil and one winding turn in Loop n of the shielding coil.

In addition, the unit flux density matrices of the three coils on the target locations are designated. For example, the unit flux density matrices in the z axis and r axis of the transmitter coil on the top boundary are defined as

$$\begin{cases}\overrightarrow{\boldsymbol{B_{zu\_top,TX}}} = [\overrightarrow{B_{zu1\_top,TX}}...\overrightarrow{B_{zuM\_top,TX}}]_{1\times M} \\ \overrightarrow{\boldsymbol{B_{ru\_top,TX}}} = [\overrightarrow{B_{ru1\_top,TX}}...\overrightarrow{B_{ruM\_top,TX}}]_{1\times M}\end{cases} \tag{6}$$

where M is the number of points on the top boundary. The unit flux density matrices of the transmitter coil on the side boundary are

$$\begin{cases}\overrightarrow{\boldsymbol{B_{zu\_side,TX}}} = [\overrightarrow{B_{zu1\_side,TX}}...\overrightarrow{B_{zuM\_side,TX}}]_{1\times K} \\ \overrightarrow{\boldsymbol{B_{ru\_side,TX}}} = [\overrightarrow{B_{ru1\_side,TX}}...\overrightarrow{B_{ruM\_side,TX}}]_{1\times K}\end{cases} \tag{7}$$

where K is the number of points on the side boundary. Similarly, the unit flux density matrices of the receiver coil are

$$\begin{cases}\overrightarrow{\boldsymbol{B_{zu\_top,RX}}} = [\overrightarrow{B_{zu1\_top,RX}}...\overrightarrow{B_{zuM\_top,RX}}]_{1\times M} \\ \overrightarrow{\boldsymbol{B_{ru\_top,RX}}} = [\overrightarrow{B_{ru1\_top,RX}}...\overrightarrow{B_{ruM\_top,RX}}]_{1\times M}\end{cases} \tag{8}$$

$$\begin{cases}\overrightarrow{\boldsymbol{B_{zu\_side,TX}}} = [\overrightarrow{B_{zu1\_side,TX}} \ldots \overrightarrow{B_{zuM\_side,TX}}]_{1\times K} \\ \overrightarrow{\boldsymbol{B_{ru\_side,TX}}} = [\overrightarrow{B_{ru1\_side,TX}} \ldots \overrightarrow{B_{ruM\_side,TX}}]_{1\times K}\end{cases} \tag{9}$$

And the unit flux density matrices of the shielding coil are

$$\overrightarrow{\boldsymbol{B_{zu\_top,SX}}} = \begin{bmatrix} \overrightarrow{B_{zu11\_top,SX}} & .. & \overrightarrow{B_{zu1N\_top,SX}} \\ : & .. & : \\ \overrightarrow{B_{zuM1\_top,SX}} & .. & \overrightarrow{B_{zuMN\_top,SX}} \end{bmatrix}_{M\times N} \tag{10}$$

$$\overrightarrow{\boldsymbol{B_{ru\_top,SX}}} = \begin{bmatrix} \overrightarrow{B_{ru11\_top,SX}} & .. & \overrightarrow{B_{ru1N\_top,SX}} \\ : & .. & : \\ \overrightarrow{B_{ruM1\_top,SX}} & .. & \overrightarrow{B_{ruMN\_top,SX}} \end{bmatrix}_{M\times N} \tag{11}$$

$$\overrightarrow{\boldsymbol{B_{zu\_side,SX}}} = \begin{bmatrix} \overrightarrow{B_{zu11\_side,SX}} & .. & \overrightarrow{B_{zu1N\_side,SX}} \\ : & .. & : \\ \overrightarrow{B_{zuK1\_side,SX}} & .. & \overrightarrow{B_{zuKN\_side,SX}} \end{bmatrix}_{K\times N} \tag{12}$$

$$\overrightarrow{\boldsymbol{B_{ru\_side,SX}}} = \begin{bmatrix} \overrightarrow{B_{ru11\_side,SX}} & .. & \overrightarrow{B_{ru1N\_side,SX}} \\ : & .. & : \\ \overrightarrow{B_{ruK1\_side,SX}} & .. & \overrightarrow{B_{ruKN\_side,SX}} \end{bmatrix}_{K\times N} \tag{13}$$

All these permeance matrices and flux density matrices are derived from the finite element analysis (FEA) simulation of the coil model shown in Fig. 2 with one turn for each Loop and 1 A per turn.

C. Mathematical Calculation of the Three-Coil Circuit

Fig. 3 shows the three-coil equivalent circuit, where $\overrightarrow{v_{TX}}$ is the fundamental component of the transmitter coil input voltage, and Z_L represents the equivalent load of the receiver coil. With an existing WPT system, it is assumed that the output power P_o, output voltage V_o, and the transmitter and receiver coil parameters (M_{TR}, $Z_{TX} = R_{TX} + j\omega L_{TX} + {}^1/_{j\omega C_{TX}}$, $Z_{RX} = R_{RX} + j\omega L_{RX} + {}^1/_{j\omega C_{RX}}$) are fixed. Hence, if the receiver-side rectifier topology is known, the receiver coil current $\overrightarrow{i_{RX}}$ and Z_L are decided.

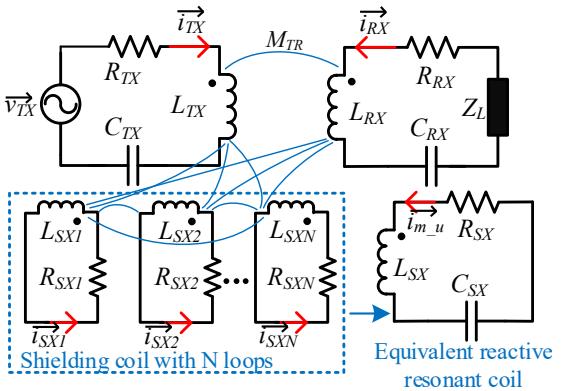

Fig. 3. Equivalent circuit of the three-coil system.

For the shielding coil, once the current vector $\boldsymbol{T_{w,SX}}$ is determined, $\overrightarrow{\boldsymbol{i_{SX}}}$ is obtained from (2), and the equivalent ESR and self-inductance of the shielding coil are calculated as

$$R_{SX} = \boldsymbol{R_{SX\_u}}|\boldsymbol{T^T_{w,SX}}| \tag{14}$$

$$L_{SX} = \boldsymbol{T_{w,SX}}\boldsymbol{L_{SX\_u}}\boldsymbol{T^T_{w,SX}} \tag{15}$$

and the equivalent mutual inductance between the shielding coil and the transmitter and receiver coils are

$$M_{TS} = \boldsymbol{M_{TS\_u}}\boldsymbol{T^T_{w,SX}} \tag{16}$$

$$M_{RS} = \boldsymbol{M_{RS\_u}}\boldsymbol{T^T_{w,SX}} \tag{17}$$

Applying KVL law on the receiver and transmitter coil circuits, the transmitter coil current $\overrightarrow{i_{TX}}$ and $\overrightarrow{v_{TX}}$ are

$$\overrightarrow{i_{TX}} = \frac{-(Z_{RX}+Z_L)\overrightarrow{i_{RX}} - \boldsymbol{Z_{RS\_u}}\overrightarrow{\boldsymbol{i^T_{SX}}}}{Z_{TR}} \tag{18}$$

$$\overrightarrow{v_{TX}} = Z_{TX}\overrightarrow{i_{TX}} + Z_{TR}\overrightarrow{i_{RX}} + \boldsymbol{Z_{TS\_u}}\overrightarrow{\boldsymbol{i^T_{SX}}} \tag{19}$$

where $Z_{TR} = j\omega M_{TR}$, $\boldsymbol{Z_{TS\_u}} = j\omega\boldsymbol{M_{TS\_u}}$, and $\boldsymbol{Z_{RS\_u}} = j\omega\boldsymbol{M_{RS\_u}}$.

With the three coil currents solved, the flux density distributed on the top boundary is estimated based on superposition

$$\begin{cases}\overrightarrow{\boldsymbol{B_{z\_top}}} = \overrightarrow{\boldsymbol{B^T_{zu\_top,TX}}}\overrightarrow{i_{TX}} + \overrightarrow{\boldsymbol{B^T_{zu\_top,RX}}}\overrightarrow{i_{RX}} \\ \qquad + \overrightarrow{\boldsymbol{B_{zu\_top,SX}}}\overrightarrow{\boldsymbol{i^T_{SX}}} \\ \overrightarrow{\boldsymbol{B_{r\_top}}} = \overrightarrow{\boldsymbol{B^T_{ru\_top,TX}}}\overrightarrow{i_{TX}} + \overrightarrow{\boldsymbol{B^T_{ru\_top,RX}}}\overrightarrow{i_{RX}} \\ \qquad + \overrightarrow{\boldsymbol{B_{ru\_top,SX}}}\overrightarrow{\boldsymbol{i^T_{SX}}} \\ \boldsymbol{B_{mag\_top}} = |\sqrt{\overrightarrow{\boldsymbol{B_{z\_top}}}^2 + \overrightarrow{\boldsymbol{B_{r\_top}}}^2}|\end{cases} \tag{20}$$

where $\boldsymbol{B_{mag\_top}}$ is the flux density magnitude on the top boundary. Similarly, the flux density distributed on the side boundary is calculated as

$$\begin{cases}\overrightarrow{\boldsymbol{B_{z\_side}}} = \overrightarrow{\boldsymbol{B^T_{zu\_side,TX}}}\overrightarrow{i_{TX}} + \overrightarrow{\boldsymbol{B^T_{zu\_side,RX}}}\overrightarrow{i_{RX}} \\ \qquad + \overrightarrow{\boldsymbol{B_{zu\_side,SX}}}\overrightarrow{\boldsymbol{i^T_{SX}}} \\ \overrightarrow{\boldsymbol{B_{r\_side}}} = \overrightarrow{\boldsymbol{B^T_{ru\_side,TX}}}\overrightarrow{i_{TX}} + \overrightarrow{\boldsymbol{B^T_{ru\_side,RX}}}\overrightarrow{i_{RX}} \\ \qquad + \overrightarrow{\boldsymbol{B_{ru\_side,SX}}}\overrightarrow{\boldsymbol{i^T_{SX}}} \\ \boldsymbol{B_{mag\_side}} = |\sqrt{\overrightarrow{\boldsymbol{B_{z\_side}}}^2 + \overrightarrow{\boldsymbol{B_{r\_side}}}^2}|\end{cases} \tag{21}$$

In addition, the power transferred to the shielding coil is

$$P_{SX} = \frac{1}{2}Re\{\boldsymbol{Z_{TS\_u}}\overrightarrow{i_{TX}}\overrightarrow{\boldsymbol{i^{*T}_{SX}}} + \boldsymbol{Z_{RS\_u}}\overrightarrow{i_{RX}}\overrightarrow{\boldsymbol{i^{*T}_{SX}}}\} \tag{22}$$

The shielding coil base current $\overrightarrow{i_{m\_u}}$ is induced by LC resonance, so compensation capacitance C_{SX} is required, which is calculated by the KVL equation of the equivalent shielding coil circuit as

$$C_{sx} = \frac{{}^j/_\omega}{R_{SX} + j\omega L_{SX} + (j\omega M_{TS}\overrightarrow{i_{TX}} + j\omega M_{RS}\overrightarrow{i_{RX}})\overrightarrow{i_{m\_u}}^{-1}} \tag{23}$$

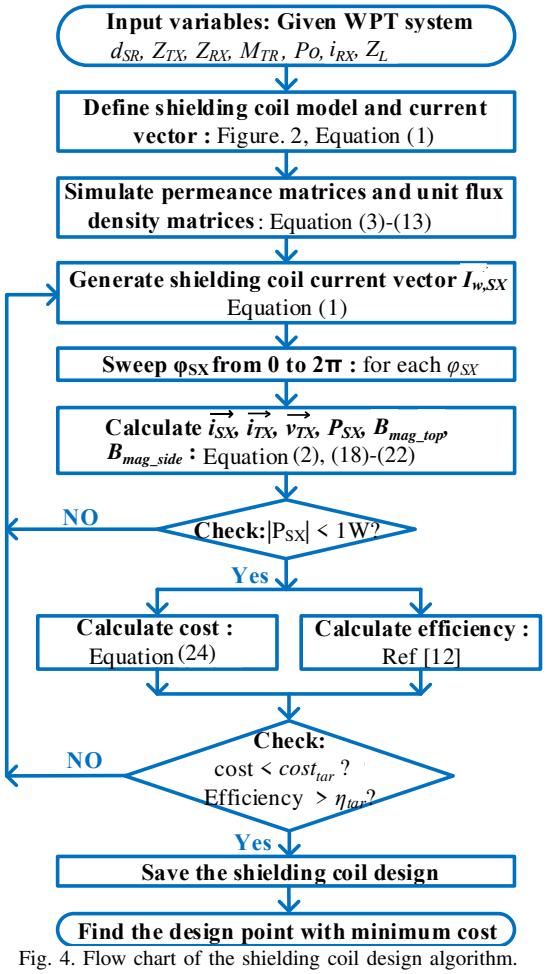

Fig. 4. Flow chart of the shielding coil design algorithm.

D. Optimized Design Algorithm of the Shielding Coil

An optimization algorithm is proposed to design the shielding coil, as illustrated in Fig. 4. The input variables define the given WPT system with fixed transmitter and receiver coils and output parameters. First, the coil model presented in Fig. 2 is identified with certain $r_{inner}, r_{outer}, d_{z,top}, d_{r,side}$, and the shielding coil loop number N and base current magnitude I_{m_u} are determined. Then, unit permeance matrices and and flux density matrices shown in (3)-(13) of the three coils are derived through FEA simulation with unit current excitation. Next, varying shielding coil current vectors are generated and current phase angle is swept from 0 to 2π. For each current phase angle, the shielding coil current $\overrightarrow{\boldsymbol{i_{SX}}}$ is composed in the form of (2). The transmitter coil current $\overrightarrow{i_{TX}}$, transmitter coil voltage $\overrightarrow{v_{TX}}$, flux densities on the target areas, and the real power of the shielding coil are calculated based on (18)-(22).

For the resonant reactive shielding coil, only ESR loss contributes to the real power. So the the power transmitted to the shielding coil should be zero in the ideal case, and cases with $|P_{SX}| < 1$ W are considered. To evaluate the shielding performance, an objective cost function of the magnetic field is defined as

$$\begin{aligned} cost &= k_{top}B_{nom,top} + k_{side}B_{nom,side} \\ &= k_{top}\Sigma_{m=1}^{M}(\frac{\boldsymbol{B_{mag\_top}}}{B_{lim}}) + k_{side}\Sigma_{k=1}^{K}(\frac{\boldsymbol{B_{mag\_side}}}{B_{lim}}) \end{aligned} \tag{24}$$

where k_{top}, k_{side} are the weighing factors imposed on the top and side area field reductions, $B_{nom,top}$, $B_{nom,side}$ are the flux density magnitudes normalized by the standard limit on the top and side areas. Smaller cost is desired for achieving a better field attenuation.

Meanwhile, power loss of the WPT system is estimated to ensure a reasonable system efficiency with the shielding coil. Here, power loss model shown in [12] is adopted for the loss estimation. Design cases with the cost lower than the target value $cost_{tar}$ and efficiency higher than the limit η_{tar} are saved. The final output result is the shielding coil design case with the minimum cost of the objective function.

III. Shielding Coil Prototype and Experimental Verification

The proposed design method of the shielding coil is validated on a 3.03 MHz EV WPT system developed in [12]. Apart from the WPT coils, a GaN-based full-bridge inverter with zero voltage switching (ZVS) is adopted on the transmitter side, and a SiC shottky diode rectifier is used on the receiver side. Based on the design procedure in Fig. 4, a shielding coil prototype is designed for the EV WPT system at 500 W output power. Since the flux density in side area is much smaller than that in the top area, the weighing factors are set as $k_{top} = 0.9, k_{side} = 0.1$. Design parameters of the WPT system and the shielding coil are presented in Table I.

TABLE I. Design parameters of the WPT system and the shielding coil.

Parameters of the original WPT system at 500 W output	
WPT coils outer radius	$r_{TX} = r_{RX} = 0.2$ m
Air gap between TX and RX	$d_{TR} = 0.1$ m
Output voltage, V_o	245 V
Load resistance, R_L	120 Ω
TX current, $\overrightarrow{i_{TX}}$	$9\angle 56.7°$ A
RX current, $\overrightarrow{i_{RX}}$	$4.35\angle 0°$ A
Converter efficiency	$\eta = 93.5\%$
Parameters of the WPT system with shielding coil at 500 W output	
Shielding coil model radius	$r_{inner} = 0.02$m, $r_{outer} = 0.22$m
Air gap between SX and RX	$d_{SR} = 0.01$ m
Current vector definition	$I_{m\_u} = 3$ A, $T_{w\_max} = 3$, $N = 11$
Height of the top boundary	$d_{z,top} = 0.1$ m
Width of the side boundary	$d_{r,side} = 0.5$ m
Target efficiency	$\eta_{tar} = 93.5\%$
TX current, $\overrightarrow{i_{TX}}$	$9.9\angle 50.5°$ A
RX current, $\overrightarrow{i_{RX}}$	$4.35\angle 0°$ A
SX current, $\overrightarrow{\boldsymbol{i_{SX}}}$	$[9\ 3\ 0\ 3\ 6\ 0\ 0\ 6\ -6\ -3\ 0]\angle 20°$ A
SX impedance	$L_{SX} = 12$ μH, $R_{SX} = 1$ Ω $C_{SX} = 240$ pF

A. Hardware Implementation

The shielding coil prototype is made with AWG 16 copper wire and compensation capacitors. Fig. 5 shows the experi-

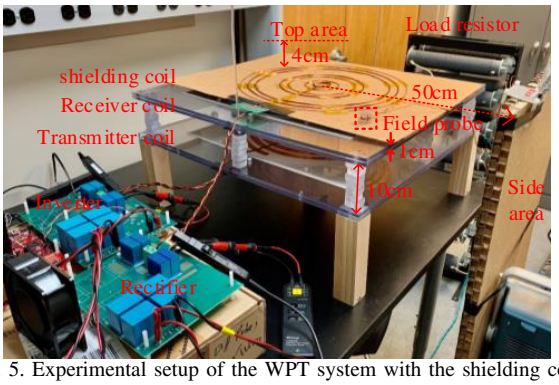

Fig. 5. Experimental setup of the WPT system with the shielding coil.

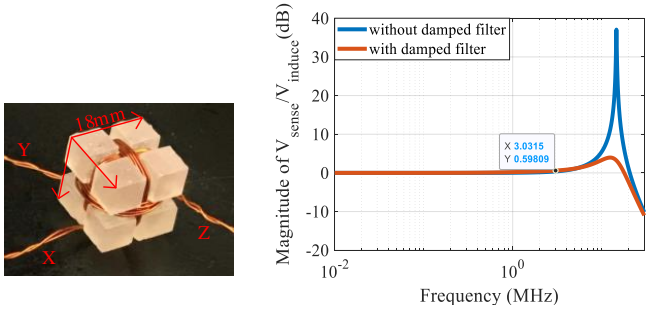

(a) (b)

Fig. 6. (a) Field probe; (b) Probe winding impedance magnitude.

mental setup of the WPT system. The shielding coil is held by a MDF board and placed above the receiver coil.

To measure the magnetic field, a field probe is fabricated following the design principle in [13], as presented in Fig. 6(a). Flux density is detected by measuring the induced voltage on three sensor windings, which are arranged perpendicularly on a cubic supporter made by a 3D printer. In each direction, the sensor winding is made by eight-turn AWG 24 copper wires. Since the WPT system operates at 3.03 MHz switching frequency, probe winding impedance shuld be checked to ensure the sufficient measurement bandwidth. Also, to avoid the impact of high-order harmonics, RC damped filter is designed to be paralleled with the probe winding for gaining a lower peak magnitude, as shown in Fig. 6(b).

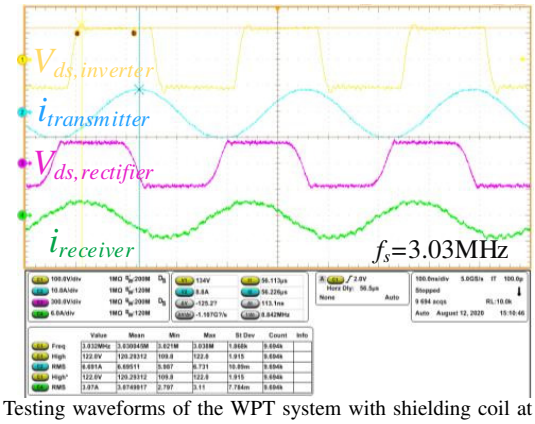

Fig. 7. Testing waveforms of the WPT system with shielding coil at 500 W.

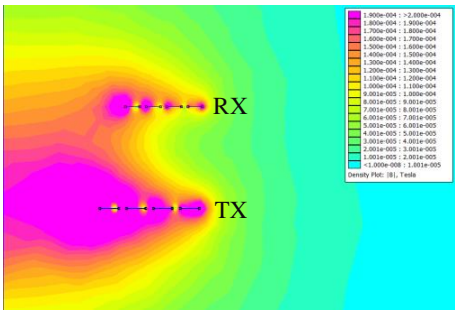

(a)

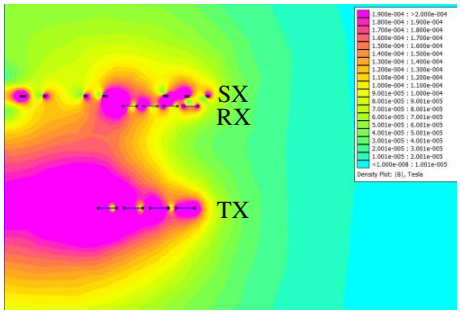

(b)

Fig. 8. Simulated flux density in FEMM at 500 W. (a) Two-coil system; (b) Three-coil system.

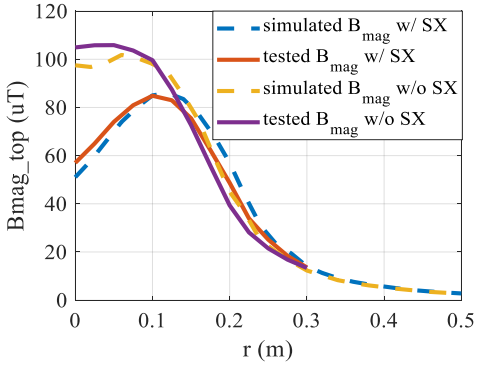

(a)

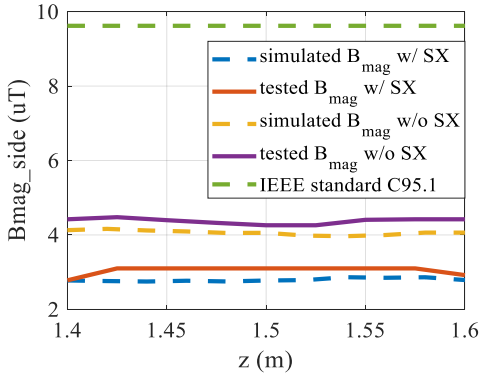

(b)

Fig. 9. (a) Tested and simulated B_{mag} on the top boundary; (b) Tested and simulated B_{mag} on the side boundary.

B. Simulation and Experimental Results

Fig. 7 shows the testing waveforms of the WPT system with the shielding coil at 500 W. The measured coil currents are $i_{TX} = 9.8\angle 53°$ A, $i_{RX} = 4.34\angle 0°$ A, which match well

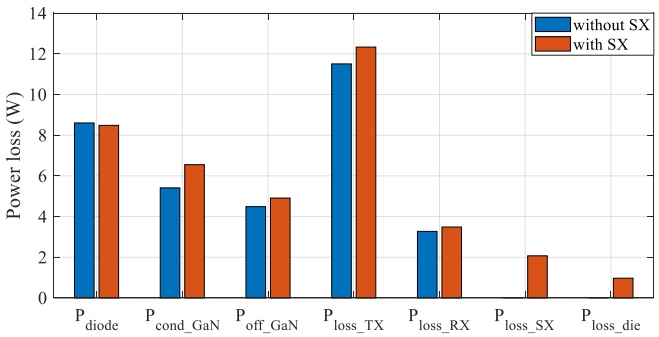

Fig. 10. Loss breakdown comparison of the WPT system at 500 W with and without the shielding coil.

with the designed values. Magnetic fields of the WPT coils with and without the shielding coil are simulated in FEMM as shown in Fig. 8, and also measured by the field probe in the experiments. Fig. 9 shows the tested and simulated flux density magnitudes on the top and side areas. As shown in Fig. 9(a), the flux density on the top-center area is significantly attenuated where the peak value is reduced from 105 μT to 50 μT. The magnetic field on the side area is maintained well below the standard, as shown in Fig. 9(b). In both cases with and without the shielding coil, the measured field is consistent with the FEMM simulation, which verifies the accuracy of of the proposed modeling.

The tested system efficiency with the shielding coil is 92.7% with 39.4 W loss, which is 0.8% lower than the original system efficiency with 34.4 W loss. Fig. 10 shows the loss breakdown of the WPT system at 500 W output power. Compared with the original system without the shielding coil, the additional power loss comes from the increased device loss and coil losses due to the changed current, and the extra 2 W loss of the shielding coil. Also, the shielding coil is embedded in a MDF coil former, which has higher loss tangent and leads to 1 W dielectric loss.

IV. Effect of the Shielding Coil in WPT System with Ferrite and Metal Plates

The proposed shielding coil has been validated in Section III, which can effectively attenuate the stray magnetic field but cannot suppress the top-side field all below the standard. Hence, traditional metal and ferrite shielding plates may still be required, especially for the EV application. In this section, influences of the shielding coil on WPT system efficiency and magnetic field are investigated. The study is still based on the EV WPT system introduced in Section III, and Al and 4F1 ferrite shielding plates are added.

A. WPT Systems with Ferrite and Al Plates

Four different implementations of the WPT system are designed, as presented in Fig. 11. In each implementation, the transmitter and receiver coil design, airgap, and alignment are unchanged. System 1 is the normal WPT system without shielding coil, and ferrite plates are placed close to the coils with a small air gap. As a comparison, in System 2, the air

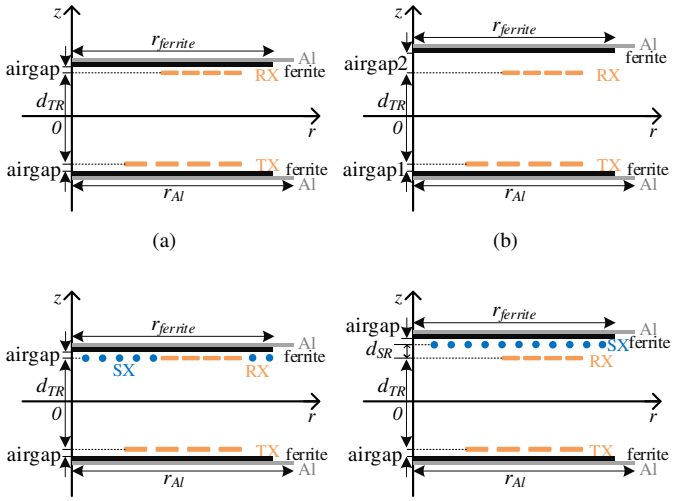

Fig. 11. Cylindrical view of WPT systems with Ferrite and Al plates where $d_{TR} = 100$ mm, $r_{ferrite} = 230$ mm, $r_{Al} = 304.8$ mm, Al plate thickness = 2.286 mm, ferrite plate thickness = 3 mm. (a) System 1: no shielding coil, airgap = 3 mm; (b) System 2: no shielding coil, airgap1 = 3 mm, airgap2 = 13 mm; (c) System 3: with shielding coil at the same z-height with the receiver coil, airgap = 3 mm; (d) System 4: with shielding coil, $d_{SR} = 10$ mm, airgap = 3 mm.

gap between the receiver coil and the ferrite plate is purposely enlarged. Corresponding to System 1 and 2, System 3 and 4 are the cases with shielding coils, where the shielding coil is designed at the same z-height as the receiver coil in System 3 and 10 mm higher than the receiver coil in System 4. The shielding coil loop model is defined with $N = 7$ in System 3 and $N = 11$ in System 4. Design of the shielding coil still follows the procedures illustrated in Fig. 4, except that unit flux densities of the coils on the ferrite plates are derived instead of that on the top boundary. Also, the objective cost function becomes the ferrite core loss, and the design case with the minimum system power loss is selected. Impacted by the locations of the ferrite and Al plates, the WPT coil inductances are slightly different, as shown in Table II.

TABLE II. Coil inductances of different WPT systems.

System	1	2	3	4
TX self inductance, L_{TX}(μH)	7.1751	7.1706	7.1681	7.1235
RX self inductance, L_{RX}(μH)	9.1696	8.2096	9.1446	8.1947
Mutual inductance, M_{TR}(μH)	2.3213	2.1477	2.3191	2.1454

B. Performance Comparison

The four WPT systems are designed with the same output at $P_o = 3$ kW, $V_o = 490$ V, $R_L = 120$ Ω. Design results of the shielding coils lead to current vector $T_{w,SX} = [-1\ -1\ 0\ 0\ 2\ 0\ 0]$ in System 3 and $T_{w,SX} = [0\ 0\ 2\ -1\ 0\ 0\ 2\ 0\ 1\ -1\ 0]$ in System 4. For each system, steady-state operation currents are solved in a switching frequency range from 2.75 MHz to 3.45 MHz that ensures ZVS operation. Power loss including the coil loss, primary side GaN device conduction loss and turn-off switching loss, diode rectifier conduction loss, and the core loss of the ferrite plates are calculated. Flux densities within the ferrite plates are also predicted.

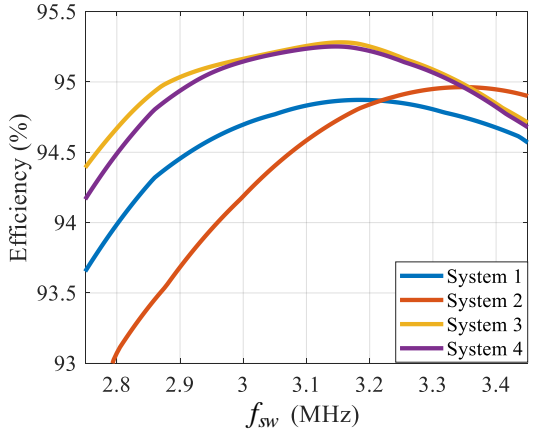

Fig. 12. System efficiencies at various switching frequencies with P_o = 3 kW, $R_L = 120\ \Omega$.

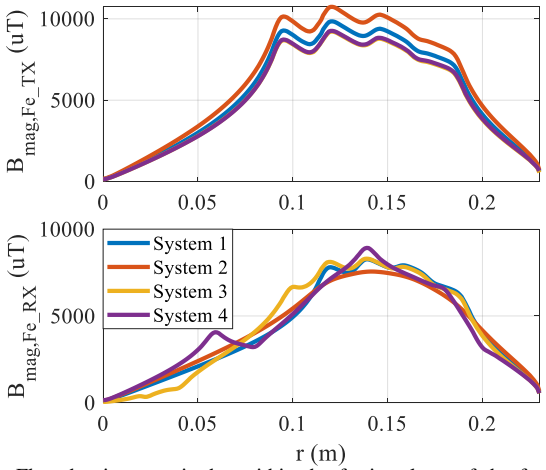

Fig. 13. Flux density magnitudes within the ferrite plates of the four WPT systems at $f_{sw} = 3.185$ MHz, $P_o = 3$ kW, $R_L = 120\ \Omega$.

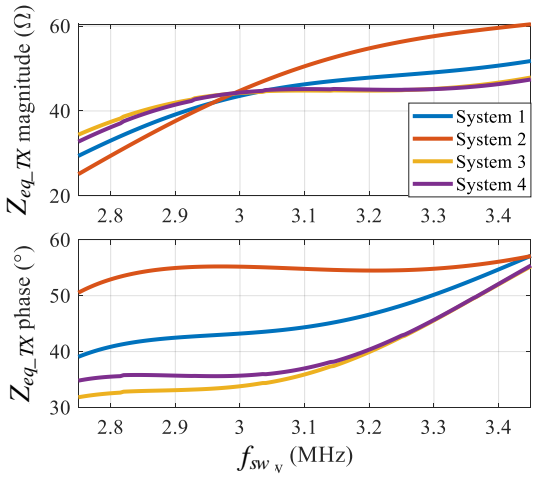

Fig. 14. Equivalent transmitter coil impedance of the WPT systems at P_o = 3 kW, $R_L = 120\ \Omega$.

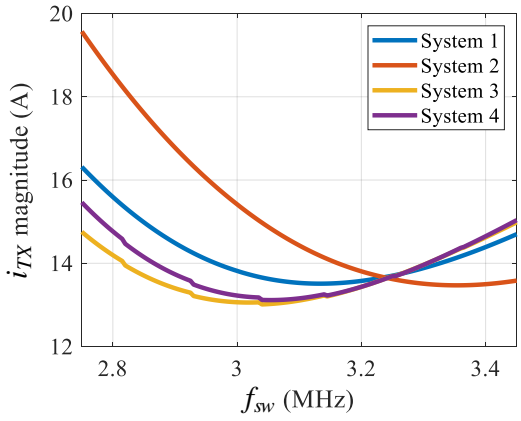

Fig. 15. Transmitter coil current magnitudes of the WPT systems at P_o = 3 kW, $R_L = 120\ \Omega$.

Fig. 12 shows the efficiency curves versus switching frequency of the four WPT systems. Implemented with shielding coils, System 3 and System 4 have higher power efficiency in most frequencies, with peak efficiency at 93%. The conventional structure in System 1 exhibits a lower power efficiency. With larger air gap in System 2, power efficiency is further reduced because of the lower coupling between WPT coils.

Fig. 13 compares the flux density magnitudes within the ferrite plates of the four WPT systems at $f_{sw} = 3.185$ MHz. Although System 3 and 4 have relatively lower power losses with shielding coils, magnetic fields within the ferrite plates are not attenuated significantly. With the shielding coils, the magnetic fields within the transmitter-side ferrite plate are reduced, and the fields in receiver-side ferrite plate are slightly reshaped but not attenuated.

To figure out the effect of the shielding coil in WPT systems, the equivalent impedance of the transmitter coil, defined as $Z_{eq\_TX} = \overrightarrow{v_{TX}}/\overrightarrow{i_{TX}}$, is calculated and compared as shown in Fig. 14, and the transmitter coil current magnitude is presented in Fig. 15. In addition, optimal efficiency of the System 1, which is regarded as the base implementation, is explored by varying the output load R_L in a wide range. It is found that System 1 achieves the maximum efficiency at 95.21% with $R_L = 93\ \Omega$, $f_{sw} = 3.06$ MHz, where $Z_{eq\_TX} = 42\angle 34°\ \Omega$.

As shown in Fig. 14, Z_{eq_TX} of System 3 and System 4 has a relatively narrow magnitude distribution and lower phase angle within the frequency range, which is closer to the optimal impedance ($Z_{eq\_TX} = 42\angle 34°\ \Omega$) of the base condition in System 1. Lower impedance phase angle also helps transfer more real power and improve the power transfer efficiency. In addition, as presented in Fig. 15, when $f_{sw} < 3.25$ MHz, System 3 and 4 with shielding coils have lower transmitter current, resulting in lower power loss. On the other hand, System 1 and System 2 have wider impedance distribution and higher phase angle, leading to higher transmitter current and lower power transfer efficiency.

Table III presents the coil currents, equivalent impedance referred to the transmitter side, and efficiency of the four WPT systems at $f_{sw} = 3.185$ MHz, $P_o = 3$ kW, $R_L = 120\ \Omega$, and Fig. 16 shows the loss comparison. By implementing the shielding coil, the WPT system efficiency is increased from

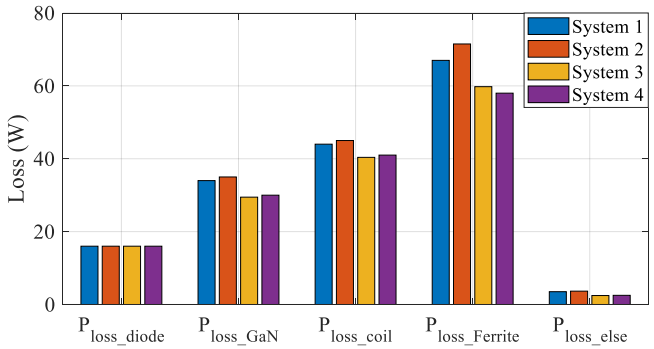

Fig. 16. Loss breakdown comparison of the four WPT systems with $f_{sw} = 3.185$ MHz, $P_o = 3$ kW, $R_L = 120\ \Omega$.

94.8% in System 1 to 95.3% in System 3 and System 4. With the same receiver current, shielding coil adjusts the equivalent transmitter impedance to achieve a lower coil current and reduce power loss, thus leading to a higher power transfer efficiency.

TABLE III. Coil currents, equivalent impedance, and power efficiencies of the WPT systems with $f_{sw} = 3.185$ MHz, $P_o = 3$ kW, $R_L = 120\ \Omega$.

System	1	2	3	4
i_{TX}(A)	$13.6\angle 109°$	$14\angle 91°$	$13\angle 118°$	$13\angle 116°$
i_{RX}(A)	10.1	10.1	10.1	10.1
$Z_{eq\_TX}(\Omega)$	$48\angle 46°$	$55\angle 55°$	$45.5\angle 39°$	$45.6\angle 40°$
Efficiency	94.8%	94.6%	95.3%	95.3%

The benefit provided by the shielding coil in this arrangement is largely limited to the specific design case employed in this study. Namely, because the transmitter and receiver coil are unchanged from a previous air-core prototype design, the addition of ferrite and metal sheets detunes the resonant tank from its designed operation. With the shielding coil, the tank impedances can be retuned closer to an impedance match for optimal efficiency. Redesigning the transmitter and receiver coil geometries for a shielded implementation, it is unlikely that the shielding coil will provide any distinct benefit in the shielded case.

V. Conclusions

In this work, effects of a resonant reactive shielding coil in an existing WPT system is investigated. A parameterized coil model that allows arbitrary circular winding geometry and current direction is proposed, and design strategy of the shielding coil with detailed modeling is developed. A shielding coil prototype is fabricated and applied on an EV WPT system, which is validated with attenuated stray magnetic field on the top area and side area. In order to investigate the effect of the shielding coil in WPT systems with ferrite/mental plates, system efficiency and magnetic field of four WPT systems with different implementation structures are evaluated. The shielding coil cannot reduce the ferrite core loss significantly by attenuating the magnetic field in this configuration. The additional coil can adjust the equivalent impedance for achieving a lower transmitter current and higher power transfer efficiency, if the base system is not already tuned to an efficiency-optimized point.

Acknowledgment

This research is supported by II-VI Foundation Block-Gift Graduate Research Program.

This work also made use of the Engineering Research Center Shared Facilities supported by the Engineering Research Center Program of the National Science Foundation and DOE under NSF Award Number EEC-1041877 and the CURENT Industry Partnership Program.

References

[1] L. Jiang and D. Costinett, "A high-efficiency GaN-based single-stage 6.78 MHz transmitter for wireless power transfer applications," *IEEE Transactions on Power Electronics*, vol. 34, no. 8, pp. 7677–7692, 2018.

[2] J. Li and D. Costinett, "Comprehensive design for 6.78 MHz wireless power transfer systems," in *IEEE Energy Conversion Congress and Exposition (ECCE)*, 2018, pp. 906–913.

[3] R. Qin and D. Costinett, "Multi-layer non-uniform series self-resonant coil for wireless power transfer," in *IEEE Energy Conversion Congress and Exposition (ECCE)*, 2019, pp. 3333–3339.

[4] D. Patil, M. K. McDonough, J. M. Miller, B. Fahimi, and P. T. Balsara, "Wireless power transfer for vehicular applications: Overview and challenges," *IEEE Transactions on Transportation Electrification*, vol. 4, no. 1, pp. 3–37, 2017.

[5] S. Y. R. Hui, W. Zhong, and C. K. Lee, "A critical review of recent progress in mid-range wireless power transfer," *IEEE Transactions on Power Electronics*, vol. 29, no. 9, pp. 4500–4511, 2013.

[6] IEEE Standards Coordinating Committee, "IEEE standard for safety levels with respect to human exposure to radio frequency electromagnetic fields, 3kHz to 300GHz," *IEEE C95. 1*, 2005.

[7] International Commission on Non-Ionizing Radiation Protection and others, "Guidelines for limiting exposure to time-varying electric and magnetic fields," *Health physics*, vol. 99, no. 6, pp. 818–836, 2010.

[8] M. Lu, "Synergetic attenuation of stray magnetic field in inductive power transfer," Ph.D. dissertation, Virginia Tech, 2017.

[9] S. Cruciani, T. Campi, F. Maradei, and M. Feliziani, "Active shielding design for wireless power transfer systems," *IEEE Transactions on Electromagnetic Compatibility*, vol. 61, no. 6, pp. 1953–1960, 2019.

[10] J. Park, D. Kim, K. Hwang, H. H. Park, S. I. Kwak, J. H. Kwon, and S. Ahn, "A resonant reactive shielding for planar wireless power transfer system in smartphone application," *IEEE Transactions on Electromagnetic Compatibility*, vol. 59, no. 2, pp. 695–703, 2017.

[11] M. Mohammad, E. T. Wodajo, S. Choi, and M. E. Elbuluk, "Modeling and design of passive shield to limit EMF emission and to minimize shield loss in unipolar wireless charging system for ev," *IEEE Transactions on Power Electronics*, vol. 34, no. 12, pp. 12 235–12 245, 2019.

[12] R. Qin, J. Li, and D. Costinett, "A high frequency wireless power transfer system for electric vehicle charging using multi-layer nonuniform self-resonant coil at MHz," in *IEEE Energy Conversion Congress and Exposition (ECCE)*, 2020, pp. 5487–5494.

[13] R. Bosshard, J. W. Kolar, and B. Wunsch, "Accurate finite-element modeling and experimental verification of inductive power transfer coil design," in *IEEE Applied Power Electronics Conference and Exposition-APEC 2014*, 2014, pp. 1648–1653.